Boundary-Layer Meteorol (2012) 142:245–263
DOI 10.1007/s10546-011-9668-3

ARTICLE

An Evaluation of Boundary-Layer Depth, Inversion and Entrainment Parameters by Large-Eddy Simulation

Ian M. Brooks · Alison M. Fowler

Received: 6 July 2011 / Accepted: 19 October 2011 / Published online: 5 November 2011

Abstract Studies of entrainment across the top of the boundary layer rely to a great extent on identification of the boundary-layer top, inversion properties, entrainment-zone depth, and the temporal changes in all of these. A variety of definitions and techniques have been used to provide automated and objective estimates; however, direct comparisons between studies is made difficult by the lack of consistency in techniques. Here we compare boundary-layer depth, entrainment-zone thickness, and entrainment rate derived from several commonly used techniques applied to a common set of large-eddy simulations of the idealized, dry, convective boundary layer. We focus in particular on those techniques applicable to lidar backscatter measurements of boundary-layer structure. We find significant differences in all the quantities of interest, and further that the behaviour as functions of common scaling parameters, such as convective Richardson number, also differ, sometimes dramatically. The discretization of the possible values of some quantities imposed by the vertical grid is found to affect some of the results even when changes to model resolution does not affect the entrainment rate or scaling behaviour. This is a particular problem where entrainment parameters are derived from a single mean profile (e.g. the buoyancy-flux profile), but not where they are derived from the statistical properties of large numbers of individual profiles (e.g. the probability distribution of the local boundary-layer top at each model grid point).

Keywords Entrainment · Inversion · Large-eddy simulation · Mixed-layer depth

1 Introduction

Entrainment in the atmospheric boundary layer (ABL) is the process by which air is mixed down across the density interface imposed by the temperature inversion at the top of the

I. M. Brooks (✉)
School of Earth and Environment, University of Leeds, Leeds, UK
e-mail: i.brooks@see.leeds.ac.uk

A. M. Fowler
Department of Meteorology, University of Reading, Reading, UK
e-mail: a.m.fowler@reading.ac.uk

ABL and incorporated into it. It is the primary mechanism by which the ABL depth increases (Boers et al. 1984) and plays a key role in determining the distribution and structure of stratiform cloud (Nicholls and Turton 1986). Its impact on stratocumulus makes entrainment an important factor influencing the global radiation budget; it is thus important to represent it accurately within large-scale models (Stevens 2002). The fundamental physical processes governing entrainment, however, and their relationships with other ABL properties, remain poorly understood. The treatment of entrainment is generally oversimplified (Angevine 2007) and it is poorly represented within numerical models (Ayotte et al. 1996; Fedorovich et al. 2004).

A significant difficulty for observational studies of entrainment is that it cannot be measured directly but must be inferred from other measurements (Lenschow et al. 1999). Laboratory studies by Deardorff et al. (1980) demonstrated a strong relationship between the normalized depth of the entrainment zone (EZ)—that region in which active mixing between the two layers takes place—and the normalized entrainment rate, both having a linear dependence on a convective Richardson number. Deardorff et al. characterized the entrainment zone by the distortion of the interface separating the two fluid layers. Observationally, the interface between the ABL and the air above is readily measured by various remote sensing techniques such as sodar (Coulter 1979; Beyrich 1997; Beyrich and Gryning 1998; Wiegner et al. 2006), radar profilers (Angevine et al. 1994; Cohn and Angevine 2000; Yi et al. 2001), and lidar (Boers et al. 1984; Melfi et al. 1985; Boers and Eloranta 1986; Piironen and Eloranta 1995; Flamant et al. 1997; Davis et al. 1997, 2000; Steyn et al. 1999; Hägeli et al. 2000; Cohn and Angevine 2000; Lammert and Bösenberg 2006; Hennemuth and Lammert 2006; Sicard et al. 2006; Wiegner et al. 2006; Träumner et al. 2011). Remote measurement of the entrainment-zone structure is thus an attractive approach for observational studies of entrainment.

Although entrainment-zone structure—usually defined simply in terms of EZ thickness—is considered a key parameter, there is no single, universally accepted definition of the entrainment zone or means of identifying it from the observations. Different definitions or methods of determining the EZ depth can produce very different values when applied to the same dataset. The multitude of approaches to determining EZ depth adds to the confusion of determining the relationship between the EZ, entrainment rate, and other ABL quantities, and can make it difficult to compare the results from different studies. No systematic study of the differences between the various approaches has been made. Here we examine how the different definitions perform and how their scaling behaviours differ for a common set of large-eddy simulations of the dry convective boundary layer.

2 The Entrainment Zone

The EZ can be defined theoretically as the region around the ABL top in which the mean buoyancy flux is negative—that is, the region where turbulent kinetic energy is being used to mix air down across the density interface. This definition is of limited use in observational studies since it is rarely, if ever, possible to measure flux profiles with adequate precision (Cohn and Angevine 2000); it is, however, readily determined within large-eddy simulations (LES). In terms of scalar quantities that are more readily measured several definitions of the EZ have been used. For simple cases the EZ can be defined as the region over which the mean profile of some scalar quantity—such as potential temperature, water vapour mixing ratio, or aerosol concentration, and hence lidar backscatter—has a significant vertical gradient (Cohn and Angevine 2000). Deardorff et al. (1980) conducted a series of laboratory

studies of convective entrainment and found that the upper limit of the entrainment zone—defined as the region of negative buoyancy flux—coincided with the greatest height reached by a very small fraction of the overshooting mixed-layer elements at any given time, while the lower limit coincided with the level where mixed-layer fluid occupied between 90 and 95% of the horizontal area. Note that, while the upper limit of the entrainment zone is well defined in this manner, the lower limit is rather less so because of the intense mixing within the ABL. These results have been used as the basis for an entrainment-zone definition used in many lidar studies, expressed in terms of the probability distribution function (PDF) of spatially (or temporally) distributed estimates of the local height of the interface between the ABL and the air above. The precise limiting values have varied slightly between studies (e.g. Wilde et al. 1985; Melfi et al. 1985; Flamant et al. 1997; Träumner et al. 2011), but the 5% and 95% levels are common and in general agreement with Deardorff et al. (1980) original results.

A potential cause of discrepancies between studies concerns the differences in the definitions of, and approaches used to identify, the local estimates of ABL top. Some early studies used visual estimates based on time-height plots of lidar backscatter (Boers et al. 1984; Boers and Eloranta 1986; Nelson et al. 1989; Ferrare et al. 1991). The simplest automated approach has been the use of a threshold value in the lidar backscatter signal (Melfi et al. 1985; Boers et al. 1988; Kiemle et al. 1998), but this requires prior knowledge of the appropriate threshold and has problems if the signal levels change within the dataset under consideration. Determination of the minimum (largest negative value) in the vertical gradient of the backscatter is an attractive approach, but small-scale structure and sample-to-sample noise can produce large gradients unrelated to the large-scale ABL structure, necessitating filtering or averaging of the data (Flamant et al. 1997; Lammert and Bösenberg 2006; Wiegner et al. 2006), which necessarily also degrades the fidelity of the representation of the larger scale structures of interest. Steyn et al. (1999) proposed a method in which a function representing an idealized lidar backscatter profile is fitted to the observed profile and mean ABL depth and entrainment-zone limits diagnosed. This approach has the advantage of using information from the whole profile, minimizing the influence of the small-scale structures that complicate the gradient technique. However, Hägeli et al. (2000) found that, while it was effective for well-mixed cases, which approximate the idealized profile, it produced 'quantitatively unrealistic' results for more complex backscatter profiles. Several recent studies have used an edge-detecting wavelet technique (Davis et al. 1997; Russell et al. 1998; Cohn and Angevine 2000; Davis et al. 2000) to determine the ABL top—ideally this finds a point at or very close to the peak in the vertical gradient in backscatter, and has the advantage of not being influenced by small-scale structure or noise in the profile. However, it may suffer bias due to large-scale vertical gradients in the signal above or below the transition zone. Brooks (2003) extended the wavelet approach to use multiple dilations and to identify both the upper and lower limits of the transition zone in a robust manner. In essence this approach utilizes a wavelet of large dilation to identify the region within which the transition zone lies for individual backscatter profiles, and then a small dilation wavelet to determine the precise altitudes of its upper and lower limits. Brooks and Fowler (2007) applied this method to tracer profiles from large-eddy simulations, and the approach has since been further refined by Grabon et al. (2010). Morille et al. (2007) utilized related wavelet techniques to identify the ABL top along with cloud and other aerosol layers within the atmosphere.

The entrainment rate is commonly expressed as an entrainment velocity, w_e, defined as the rate of change of altitude of the mean ABL top (adjusted for the influence of large-scale subsidence). As with the entrainment zone, there are different definitions of ABL top and

methods of determining it from the observations, not all of which agree closely. Some commonly adopted definitions of ABL depth are: the level at which the mean buoyancy flux is a minimum (Deardorff et al. 1980; Sullivan et al. 1998); the mean of the local boundary-layer tops determined via gradient or wavelet techniques (Sullivan et al. 1998; Cohn and Angevine 2000); and the height of the maximum in a profile of the variance in some scalar quantity (Piironen and Eloranta 1995; Lammert and Bösenberg 2006; Hennemuth and Lammert 2006).

Davis et al. (1997) have argued that an EZ depth determined from the statistics of local ABL top estimates does not properly characterize the entrainment zone since entrainment is an inherently local phenomenon—air is mixed across the inversion in discrete events associated with overturning eddies or the pinching off of free tropospheric air drawn down into the ABL around the edges of large eddies (Sullivan et al. 1998). Such entrainment events may be separated both spatially and temporally; entrainment may thus be considered to be a discontinuous process. The entrainment velocity, however, is by definition an area- and time-averaged property of the ABL.

A note on terminology: throughout this paper the term 'inversion' will refer strictly to the temperature inversion. The local region across which lidar backscatter or tracer concentration changes from the well-mixed value within the boundary layer to its free tropospheric value will be referred to as the 'transition zone'. The term 'entrainment zone' will refer to the area-averaged vertical interval in which entrainment mixing is assumed to be active as defined by any of the definitions under consideration.

3 Large-Eddy Simulations

The results presented here are drawn from a series of large-eddy simulations of a dry convective atmospheric boundary layer conducted with the Boussinesq version of the UK Met Office Large Eddy Model (LEM) (v2.3) using its standard subgrid model (Lock and Macvean 1999). The LEM has been used successfully in a number of previous studies of entrainment (Lock 1998; Lock and Macvean 1999; Brooks and Fowler 2007). Most of the simulations were run on a $100 \times 100 \times 100$ grid with a horizontal grid spacing of 50 m. The vertical grid is stretchable, and varied smoothly between a resolution of approximately 25 m in the lower part of the ABL, through a maximum resolution of 12 m in the region around the entrainment zone—from about 100 m below the initial inversion up to approximately twice the ABL depth—and increasing to 110 m near the top of the domain at 3 km. This is comparable with the grid spacing used in previous studies of entrainment in free convective conditions (e.g. Sullivan et al. 1998). A number of additional simulations were conducted with finer ($\Delta x = \Delta y = 25$ m, $\Delta z_{\min} = 7.3$ m) or coarser ($\Delta z_{\min} = 22.9$ m) grids to assess the sensitivity of the results to grid resolution, or out of necessity where the default grid resolution was found to be inadequate for a particular set of conditions. Where cases have been repeated at different grid resolutions the highest available resolution has been used throughout the main part of the study. The simulations were initialized with potential temperature profiles of a constant 300 K within the ABL, an inversion layer 50 or 100 m deep with temperature jumps of between 1 and 10 K, and a constant lapse rate of 3 K km^{-1} above the ABL. A passive tracer, Q, was initially set to a constant value within the ABL, decreasing linearly to zero across the inversion. The surface heat flux was specified as a constant for each simulation, and a small random perturbation added to the initial potential temperature field within the boundary layer to initialize turbulence. Approximately two hours of simulated time were required for turbulence to become fully developed and the initial inversion to be modified by

Table 1 Simulation initial conditions

RUN ID	Symbol	Initial $\Delta\theta$ (K)	$\overline{w'\theta'_s}$ (W m^{-2}) ($\overline{w'\theta'_s}$ (K m s^{-1}))	Notes
A	△	1	50 (0.0425)	
B	▽	1	35 (0.0298)	
C	▲	1	10 (0.0085)	
D	◇	2	20 (0.0170)	$\Delta z_{\min} = 7.27$ m, $100 \times 100 \times 150$ grid
E	□	2	40 (0.0340)	
(F)	■	2	40 (0.0340)	Initial $z_i = 300$ m
G	♦	2	60 (0.0511)	
H	○	2	80 (0.0682)	
I	★	2	30 (0.0255)	
(J)	×	4	10 (0.0085)	
K	+	4	80 (0.0682)	
L	▷	1	20 (0.0170)	$\Delta x = \Delta y = 25$ m, $\Delta z_{\min} = 7.27$ m on $200 \times 200 \times 150$ grid
(N)	▷	1	20 (0.0170)	
O	∗	10	100 (0.0854)	$\Delta x = \Delta y = 25$ m, $\Delta z_{\min} = 7.27$ m on $200 \times 200 \times 150$ grid
P	■	2	40 (0.0340)	As run F but with $\Delta x = \Delta y = 25$ m, $\Delta z_{\min} = 7.27$ m on $200 \times 200 \times 150$ grid
Q	×	4	10 (0.0085)	As run J with $\Delta x = \Delta y = 25$ m, $\Delta z_{\min} = 7.27$ m on $200 \times 200 \times 150$ grid
(R)	◇	2	20 (0.0170)	
(S)	∗	10	100 (0.0854)	

Model grid is $\Delta x = \Delta y = 50$ m, $\Delta z_{\min} = 12$ m on $100 \times 100 \times 100$ grid except where noted; initial $z_i = 650$ m and inversion depth = 50 m except where noted. Entries in brackets (F, J, N, R, S) are used only for resolution sensitivity tests—their symbols match those for the corresponding runs at higher resolution, but in grey

entrainment so that its structure was fully determined by the forcing conditions. After this time diagnostic output files were saved at regular intervals of 15 min for a period of between 3 and 6 hours. Diagnostics included time series of domain-averaged quantities, vertical profiles averaged over both the horizontal domain and the time interval since the last output file, and three-dimensional (3D) fields of the instantaneous values of potential temperature, passive tracer concentration, and wind velocity components. The initial conditions for each simulation are summarized in Table 1; most of these simulations (cases A–O) were also used by Brooks and Fowler (2007).

4 Comparison of Definitions

Different techniques for determining ABL top and entrainment-zone depth from remote sensing data respond to different features in the signal profile and to some extent to different physical processes, and can produce significantly different results for the same dataset. Figure 1 illustrates some of these differences. The region of negative buoyancy flux defines a layer 258 m deep, much greater than the 138 m defined by the 5–95% limits of the PDF of

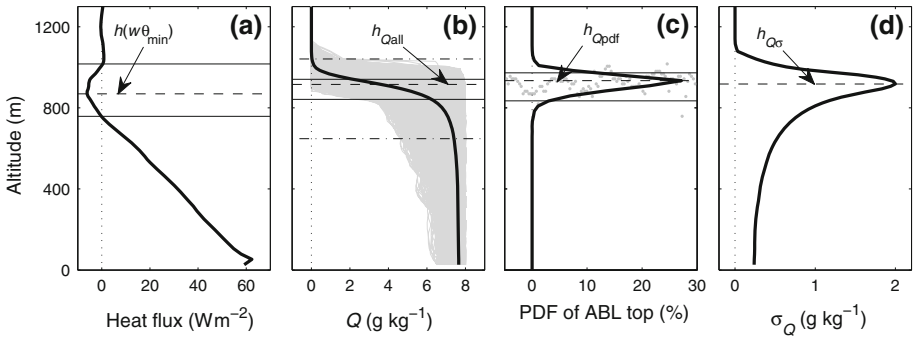

Fig. 1 Example profiles and entrainment-zone limits from simulation G at time = 5.25 h. In each panel the *horizontal dashed line* indicates an estimate of ABL top, the *solid horizontal lines* indicate entrainment-zone limits. **a** The resolved temperature (buoyancy) flux, ABL top is determined from the level of the minimum flux, and entrainment-zone limits are defined by the region of negative flux; **b** profiles of the passive tracer at each horizontal grid point (*grey*), the horizontally domain-averaged profile (*thick black line*), the entrainment-zone limits are determined from the means of the individual profile transition-zone limits, and ABL top is the mean of the levels of maximum wavelet covariance for the individual profiles. The *horizontal dash-dotted lines* indicate an entrainment zone estimated as the region of significant vertical gradient (2.5% of peak gradient) in the domain-averaged profile. **c** The probability distribution for individual ABL top estimates (the level of the peak gradient in each tracer profile); mean ABL top is estimated as the level of the peak in the probability distribution; entrainment-zone limits are the 5 and 95% limits of the probability distribution. The *grey dots* show individual ABL top estimates for a single cross-section through the model domain. **d** Profile of the standard deviation of tracer concentration in a *horizontal plane*; ABL top is estimated as the level of the maximum standard deviation

ABL top estimates. There is no clear definition of what constitutes a 'significant' gradient to define the entrainment zone from a mean scalar profile; the values indicated on Fig. 1 were chosen subjectively by visually selecting the upper limit of the well-mixed layer. They correspond to 2.5% of the peak gradient, and define a layer 393 m deep. The boundary-layer top estimates also differ (see Sect. 4.1 and Table 2 for details): the minimum in the heat flux profile is the lowest at 869 m, the peak in the gradient of the mean Q profile (not shown) and in the standard deviation of Q both lie at 918 m, while the mean of the ABL top estimates from individual Q profiles is at 924 m and the level of the peak in the probability distribution of these individual ABL top estimates is at 934 m. These values span a range of 55 m, about 6% of the mean value. Below we compare the different methods of determining ABL and entrainment parameters in more detail. With the exception of the buoyancy flux, we focus on methods that could be applied to lidar backscatter studies. Where a wavelet algorithm is utilized we have used the version defined by Brooks (2003) for consistency with results presented by Brooks and Fowler (2007) using the same set of large-eddy simulations.

Throughout much of the analysis below, we use a convective Richardson number, Ri_*, and convective velocity scale, w_*, as scaling parameters. Ri_* is defined following Sullivan et al. (1998)

$$Ri_* = \frac{\Delta\theta}{\theta_*} \tag{1}$$

where $\Delta\theta$ is the mean jump in potential temperature across the inversion and θ_* is the mixed-layer temperature scale,

Table 2 Definitions of different measures of boundary-layer depth

$h(w\theta_0)$	The altitude at which the buoyancy flux first becomes zero
$h(w\theta_{\min})$	The altitude at which the buoyancy flux has its minimum
h_{Q1}	The mean altitude of the lower limits of individual transition zone estimates from the wavelet covariance algorithm ($=\langle h_1\rangle$)
h_{Q3}	The mean altitude of the maxima in the wavelet covariance transform ($=\langle h_3\rangle$)
h_{Qall}	The mean altitude of the peaks in the gradient of individual Q profiles
h_{Qavg}	The altitude of the peak gradient of the domain averaged Q profile
$h_{Q\sigma}$	The altitude of the maximum in the profile of standard deviation of Q
h_{Qpdf}	The altitude of the peak in the probability distribution function of maxima in the gradient of individual Q profiles

$$\theta_* = \frac{\overline{w'\theta'_s}}{w_*}, \tag{2}$$

$$w_* = \left[\frac{g z_i}{\overline{\theta}}\overline{w'\theta'_s}\right]^{1/3}, \tag{3}$$

where g is the acceleration due to gravity, z_i is the mean height of the inversion base, $\overline{\theta}$ is the mean temperature within the mixed layer, and $\overline{w'\theta'_s}$ is the surface kinematic heat flux. The inverse Richardson number, Ri_*^{-1}, is a measure of the relative strength of convective forcing driving entrainment to that of the inversion layer inhibiting it.

As noted above, and demonstrated below, the different methods for identifying the locations of key features of the boundary layer can return different results. For consistency we use a single definition of z_i and the levels across which $\Delta\theta$ is determined for the calculation of Ri_*. The wavelet algorithm of Brooks (2003) is used to identify the upper and lower limits of the transition zone from each individual tracer concentration profile in the model domain, z_i is then defined as the mean of the lower limits, and $\Delta\theta$ as the mean of the differences in θ between the upper and lower limits for each grid location.

4.1 Boundary-Layer Depth

Perhaps the most fundamental property of the boundary layer is its depth, and considerable effort has been invested in developing means of determining it via remote sensing techniques (Angevine et al. 1994; Beyrich 1997; Steyn et al. 1999; Cohn and Angevine 2000; Davis et al. 2000; Hägeli et al. 2000; Brooks 2003; Hennemuth and Lammert 2006; Lammert and Bösenberg 2006; Wiegner et al. 2006; Sicard et al. 2006; de Haij et al. 2007; Emeis et al. 2008; Tucker et al. 2009). It is relevant to the entrainment problem in several ways: the entrainment velocity is determined from the rate of change of the mean ABL depth, it is commonly used as a scaling length for EZ depth, and some EZ depth estimation methods rely upon estimates of the local ABL depth. As noted above, different methods may provide significantly different estimates of ABL depth. Furthermore, there are at least two physically distinct quantities loosely referred to as ABL depth: the top of the well-mixed layer or inversion base, usually

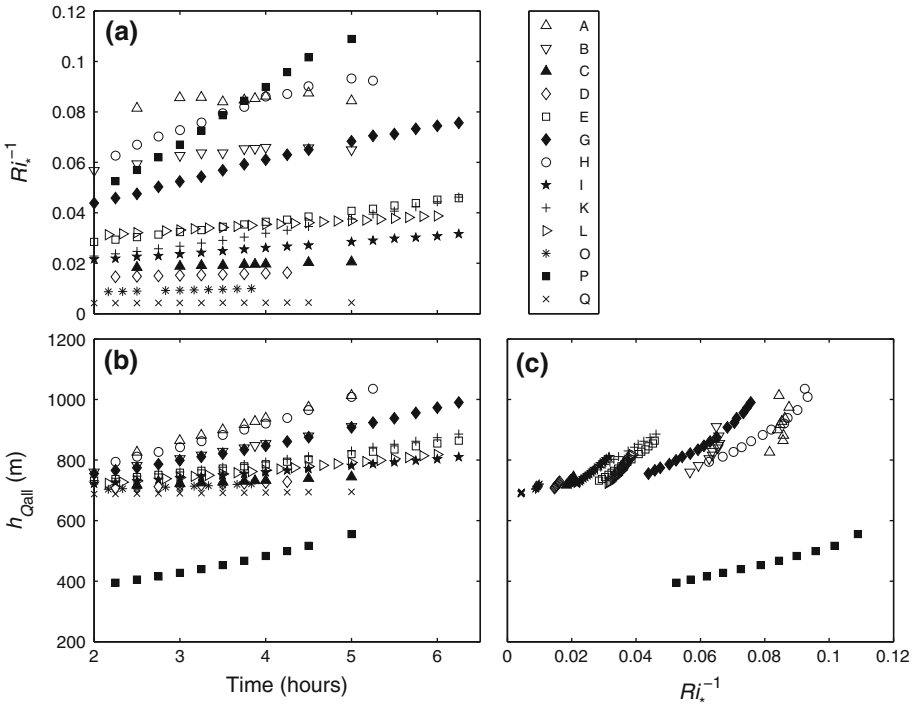

Fig. 2 The variation of **a** inverse Richardson number with time, **b** mean ABL depth (h_{Qall}) with time, and **c** h_{Qall} with inverse Richardson number. See Table 1 for details of the model configuration for each run

denoted z_{i}, and the levels given in Fig. 1, which correspond approximately to the middle of the inversion layer. The latter is also sometimes denoted z_{i}. It appears uncommon for entrainment studies to make a clear distinction between these two altitudes, although they may differ substantially. A notable exception to this is the original study of Deardorff et al. (1980), where the altitude at which the buoyancy flux first became zero (the lower limit of the entrainment zone, and approximately the top of the well-mixed layer) is used as the scaling length with which to normalize entrainment-zone depth, while the level of the minimum in the buoyancy flux (approximately the centre of the entrainment zone) is used to determine the entrainment velocity and as the length scale in the definition of the convective Richardson number.

Here we examine a number of measures of mean ABL depth, h, summarized in Table 2: h_{Q1} is a measure of the mean depth of the well-mixed layer defined as the mean of the individual estimates of transition-zone base identified by the wavelet covariance algorithm; $h(w\theta_0)$, the altitude at which the buoyancy flux first becomes zero, is also roughly comparable to the well-mixed layer depth. The other estimates of h all correspond roughly to the middle of the transition zone; $h(w\theta_{\mathrm{min}})$ is the altitude of the minimum in the buoyancy flux; h_{Q3} is the mean altitude of the maxima in the individual wavelet covariance transform profiles; h_{Qall} is the mean altitude of the peak gradients in the individual Q profiles; h_{Qavg} is the altitude of the peak gradient in the domain-averaged Q profile; and $h_{\mathrm{Q}\sigma}$ is the altitude of the maxima in the profile of the standard deviation of Q for each model level. In order to compare the different measures we scale each by h_{Qall}, chosen as the normalizing variable since this is probably the most commonly used measure of ABL depth in lidar studies. Figure 2 shows

the behaviour of Ri_*^{-1} over time, and of the boundary-layer depth estimate h_{Qall} with both time and Ri_*^{-1}. As each simulation evolves Ri_*^{-1} typically increases smoothly; this increase results primarily from a decrease in $\Delta\theta$ as the ABL warms under the combined influence of the surface heat flux and entrainment of warmer air. A smaller contribution comes from a slow decrease in θ_*, which in turn results from an increase in w_* over time. The ABL depth increases more or less smoothly in time, and at a slowly increasing rate as Ri_*^{-1} increases.

Figure 3 shows the behaviour of the different boundary-layer depth estimates scaled by h_{Qall} (3a–d,g) as functions of Ri_*^{-1}, along with similarly scaled mixed-layer depth estimates (3e,f). Linear fits to the results are also shown; the coefficients of the fits are given in Table 3. Of the five ABL depth measures four (3b–d,g) are very close to the value of h_{Qall}; h_{Q3} (3b) differs by at most 1%—less than one vertical grid interval for most of the simulations—and may be considered identical for practical purposes. There is no significant trend with Ri_*^{-1}; the four model runs with slightly higher values (D, L, O, Q) are a result of a sensitivity of the ABL depth definition to higher grid resolution (see Sect. 4.4) and are omitted from the linear fit. The heights of the peaks in mean vertical gradient (3c) and horizontal standard deviation (3d) of the tracer concentration are very similar to each other; both show a small but distinct increasing trend with Ri_*^{-1}, the gradient in (3d) being approximately double that in (3c). The scatter in each is of similar magnitude. In both cases one model run (D) stands out from the others due to a resolution dependency (see Sect. 4.4). Again, the maximum 2% difference from h_{Qall} is small in absolute terms—less than 1–2 vertical grid intervals. The level of the minimum in the buoyancy flux (3a) is significantly lower than the other ABL depth estimates, being only about 94% of h_{Qall}; Sullivan et al. (1998) found a similar difference between the level of the minimum buoyancy flux and ABL depth defined by the maximum gradient in the potential temperature. The values determined from instantaneous 3D fields (grey) show much greater scatter than those in which time averaging (black) filters out much of the short-period variability in the local fluxes; they also show a significantly different mean trend, increasing with Ri_*^{-1} whereas the time-averaged results decrease. Finally, the altitude of the peak in the PDF of the peaks in individual Q profiles (3g) is within about 2% of h_{Qall} but with a slight increasing trend with Ri_*^{-1}.

The two measures of mixed-layer depth considered differ markedly. The level at which the buoyancy flux first becomes negative (3e) has a mean of 78% of h_{Qall} for the time-averaged profiles, the values derived from instantaneous fields have a slightly higher value, greater scatter, and display a slightly stronger increasing trend with Ri_*^{-1} than that for the time-averaged results. The mean of the lower limit of the local transition zone (3f) shows a strong and well-defined trend with Ri_*^{-1}, decreasing from around 97% of mean ABL depth to around 89%. This is consistent with a deepening entrainment zone where h_{Qall} increases more rapidly than h_{Q1}.

4.2 Entrainment Rate

Entrainment velocities, calculated from the rate of change of the ABL depth (definitions discussed above), are shown in Fig. 4 normalized by w_*; lines of best fit to the results are shown and their coefficients are listed in Table 4. In all panels the fit for the case derived from h_{Qall} (4h) is also shown for reference. The values calculated from the buoyancy-flux profiles (4a,e) show the highest degree of variability; this is again higher for the instantaneous profiles than for the time-averaged profiles. The values determined from the minimum in the buoyancy flux (4a) are almost constant, with only a slight increase with Ri_*^{-1}, and with very similar trends for both time-averaged (dash-dot line) and instantaneous (solid line) fields. However,

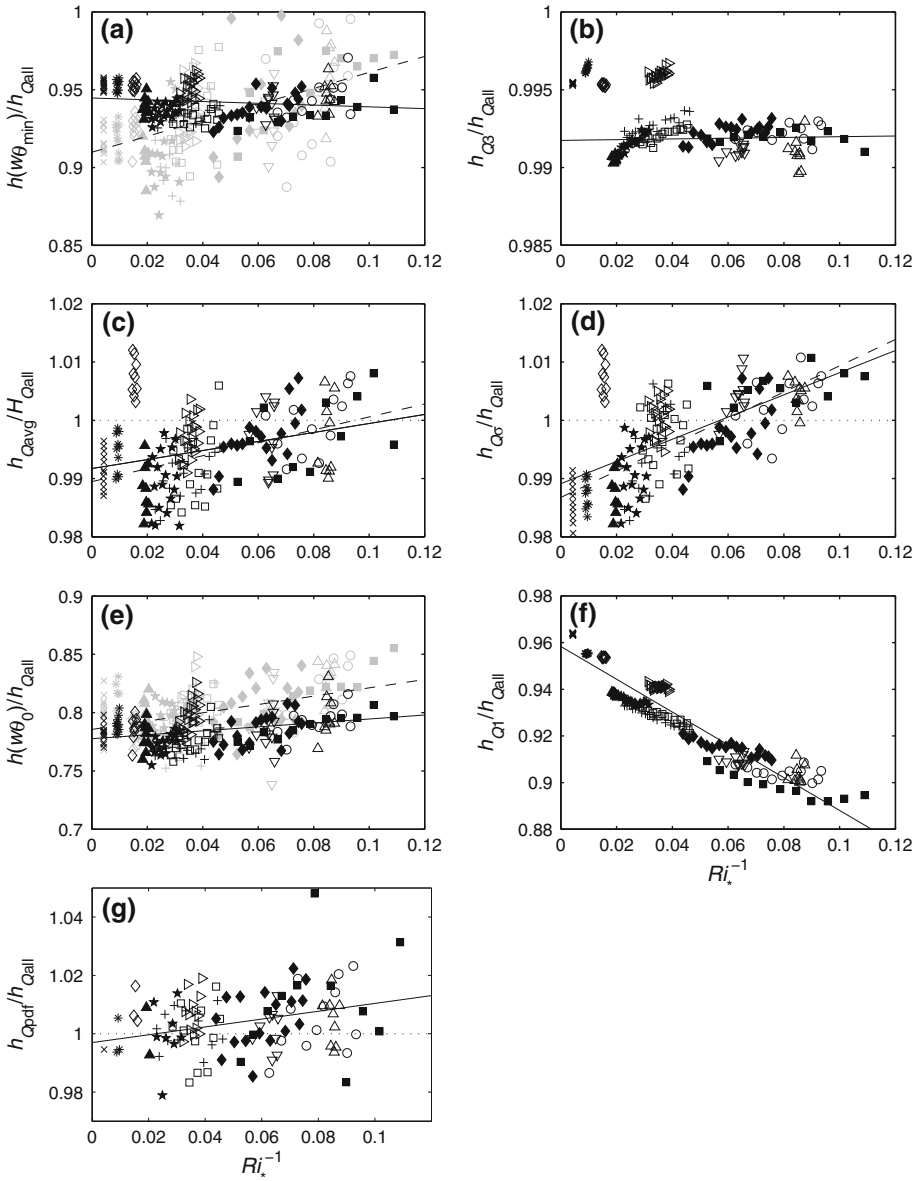

Fig. 3 Ratios of boundary-layer depth estimates to h_{Qall}: **a** height of the minimum in the buoyancy flux determined from instantaneous 3D field (*grey points*, *dash line*) and mean profiles averaged over both the horizontal domain and over the time interval since the previous 3D field output (typically 15 min) (*black points*, *solid line*); **b** height of the maximum in the wavelet covariance transform; **c** height of the peak in the vertical gradient of the horizontally domain-averaged tracer field (*solid line* is fit to all points, *dashline* is fit excluding run D); **d** height of the maximum in the standard deviation of the tracer (*solid line* is fit to all points, *dashline* is fit excluding run D); **e** height at which the buoyancy flux first becomes zero for both instantaneous 3D fields (*grey points*, *dash line*) and domain and time averaged profiles (*black points*, *solid line*); **f** mean height of the lower limit of the transition zone determined from the wavelet covariance transform; **g** height of peak in probability distribution of maxima in individual Q profiles. *Lines* are best fits to the data (see Table 3 for coefficients). Note different scales on y-axes

Table 3 Coefficients for lines of best fit in Fig. 3

Figure panel/line/dataset	Gradient	Intercept
(a) Time averaged (black, solid line)	-0.057 ± 0.057	0.945 ± 0.003
(a) Instantaneous (grey, dash line)	0.513 ± 0.126	0.910 ± 0.006
(b) Excluding runs D, L, O, Q (solid line)	0.002 ± 0.006	0.992 ± 0.0003
(c) (Solid line)	0.077 ± 0.036	0.992 ± 0.002
(c) Excluding run D (dash line)	0.111 ± 0.031	0.990 ± 0.002
(d) (Solid line)	0.190 ± 0.036	0.989 ± 0.002
(d) Excluding run D (dash line)	0.226 ± 0.030	0.987 ± 0.002
(e) Time averaged (black) (solid line)	0.170 ± 0.079	0.778 ± 0.004
(e) Instantaneous (grey) (dash line)	0.357 ± 0.112	0.786 ± 0.006
(f) (solid line)	-0.703 ± 0.038	0.958 ± 0.002
(g) (solid line)	0.134 ± 0.040	0.997 ± 0.002

Uncertainties in gradient and intercept are the 95% confidence limits

the absolute value determined from the instantaneous fields is almost double that determined from the time-averaged profiles. The values determined from the level at which the buoyancy flux first goes to zero (4e) are similar to those in Fig. 4a, but show a weak increasing trend with Ri_*^{-1} for the time-averaged fields, and a decreasing trend for the instantaneous fields. The case derived from h_{Qpdf} (4g) shows a similar behaviour to those values derived from the flux profiles—a near constant value, decreasing very slightly with Ri_*^{-1}. All the other definitions show a more pronounced increase in entrainment velocity with inverse Richardson number. Those derived from the wavelet estimates of ABL top, h_{Q3} (4b) and mixed-layer top, h_{Q1} (4f), and h_{Qall} (4h) show least scatter. The two ABL top derived estimates are very close (4b,h), while the rate of increase of mixed-layer top (4f) is slightly lower; this is consistent with an entrainment-zone depth that is proportional to the entrainment velocity. The values derived from the peak gradient in mean scalar profiles (4c), and the horizontal standard deviation of tracer concentration (4d) are very similar to each other; both display considerable scatter and both have slightly higher means than the estimates in Fig. 4b,f, and h, but have a weaker dependence on Ri_*^{-1}. The value derived from the peak in the probability distribution of individual ABL top estimates (4g) is similar to those values derived from the heat-flux profiles, but decreases slightly with Ri_*^{-1}.

Three of the normalized entrainment velocities (4c,d,g) have some individual estimates of entrainment velocity equal to zero. These cases, along with those in Fig. 4a,e, also have a weak trend with Ri_*^{-1} and do not approach zero as Ri_*^{-1} does. A common feature of these cases is that the ABL depth is determined from a single profile of a domain-averaged quantity. The ABL depth estimates from which w_{e} is determined are thus quantized by the model vertical grid—only certain values are possible. Thus, even where the mean entrainment velocity is significant, it is possible for two consecutive estimates of ABL depth to be the same and the calculated entrainment velocity to be zero. The discretization of possible ABL depth values also explains the weak mean trends in these cases; because ABL depth values are restricted by the model grid, the increase in depth between model output times is restricted to integer multiples of the grid spacing. The minimum possible entrainment velocity estimate is defined by an increase in ABL depth by one vertical grid interval—7.25 or 12 m—over the 15-min interval between model outputs, $w_{\mathrm{e}} = 0.0083$ and $w_{\mathrm{e}} = 0.0133\,\mathrm{m\,s^{-1}}$ respectively; w_* is of order $1\,\mathrm{m\,s^{-1}}$, ranging between approximately 0.55 and $1.25\,\mathrm{m\,s^{-1}}$. In the remaining cases

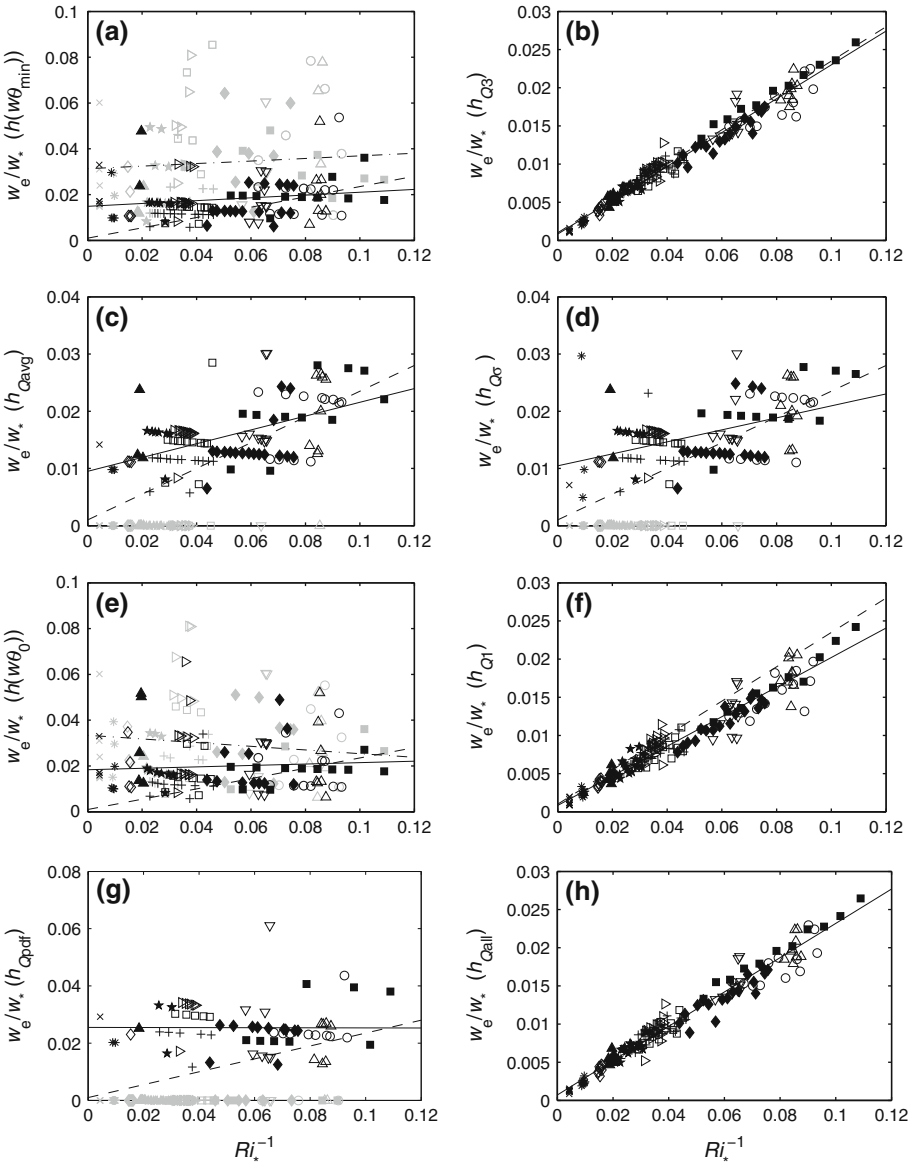

Fig. 4 Entrainment velocities scaled by the convective velocity scale w_* plotted against Ri_*^{-1}. Entrainment velocities (**a**–**f**) are defined as the rate of change of the ABL depth measures in Fig. 3a–g; **h** shows that determined from h_{Qall}. In **a** and **e** *grey/black symbols* are from instantaneous/time-averaged profiles (as Fig. 3). In **c**, **d**, **f** *grey symbols* are used wherever the calculated entrainment rate is zero. *Solid lines* are best fits to the black points; the *dash-dot line* to the *grey points* (instantaneous fields) in (**a**) and (**e**). In **c**, **d**, **f** the cases with zero entrainment (*grey points*) are not included in the data to which the *line* is fit. The *dashed lines* in (**a**–**g**) show the fit from (**h**) for reference

(4b,f,h) the ABL depth is determined from the mean of local estimates made from the profiles at each horizontal grid point—the vertical discretization applies to the individual cases, but is smoothed out by the averaging process.

Table 4 Coefficients for lines of best fit in Fig. 4

Figure panel/line/dataset	Gradient	Intercept
(a) Time averaged (black) (solid line)	0.061 ± 0.085	0.015 ± 0.005
(a) Instantaneous (grey) (dash-dot line)	0.056 ± 0.152	0.031 ± 0.008
(b) (Solid line)	0.222 ± 0.006	0.001 ± 0.0003
(c) (Solid line)	0.120 ± 0.035	0.010 ± 0.002
(d) (Solid line)	0.105 ± 0.036	0.011 ± 0.002
(e) Time averaged (black) (solid line)	0.031 ± 0.085	0.018 ± 0.005
(e) Instantaneous (grey) (dash-dot line)	-0.080 ± 0.158	0.033 ± 0.009
(f) (Solid line)	0.194 ± 0.008	0.001 ± 0.0004
(g) (Solid line)	0.002 ± 0.041	0.026 ± 0.003
(h) (Solid line)	0.225 ± 0.006	0.001 ± 0.003

4.3 Entrainment-Zone Depth

We initially consider two widely used definitions of entrainment-zone depth: the region of negative buoyancy flux and the region between the 5% and 95% limits of the probability distribution function (PDF) of individual ABL top estimates derived from scalar profiles (see Fig. 1). In some cases the determination of the region of negative buoyancy flux presents a technical problem in that the upper limit is not well-defined—the flux remains negative, though very small in magnitude, well above the upper limit of the inversion. In order to simplify the determination of the EZ limits and to maintain consistency we take advantage of the fact that the majority of the negative portion of the flux profile is approximately symmetric about the minimum, and define the EZ to be twice the depth of the region between the first zero crossing of the profile and its minimum. A self-consistent normalizing height for the flux-profile derived entrainment-zone depth is either the level of the minimum in the buoyancy flux or its first zero crossing; both are examined here. We also examine two definitions derived from the individual wavelet estimates of the local transition-zone limits: the first is the mean of the individually normalized transition-zone depths: $\langle (h_2 - h_1)/h_1 \rangle$, where h_1 and h_2 are local estimates of the lower and upper limits of the transition zone and $\langle\ \rangle$ is the averaging operator; the second is the mean of the individual transition-zone depths normalized by the mean mixed-layer depth: $\langle h_2 - h_1 \rangle / \langle h_1 \rangle$. These normalized EZ depth estimates are all shown in Fig. 5 as functions of Ri_*^{-1}; the coefficients of linear fits to the results are given in Table 5. The definitions based on the probability distribution of the local ABL depth and on the local wavelet-derived transition-zone depth (5a) show broadly similar behaviour, with the normalized EZ depth increasing with Ri_*^{-1}, though with different gradients in each case, with the PDF-derived entrainment zone having the strongest dependence on Ri_*^{-1}. The region of negative buoyancy flux (5b,c) is a much deeper layer than the other definitions of EZ depth—up to 50% of the total ABL depth—and shows much greater scatter between individual estimates, and a markedly different dependence on Richardson number. The values based on instantaneous estimates of the flux increase only slightly with Ri_*^{-1}; those determined from time-averaged profiles show less scatter, have generally higher mean values, but show a decreasing trend with Ri_*^{-1}.

In Fig. 1 we arbitrarily selected a point by eye from the mean profile of tracer concentration that represented a reasonable, if subjective, estimate of the top of the mixed layer, and used this to define a limiting gradient as a fraction of the peak gradient to represent the

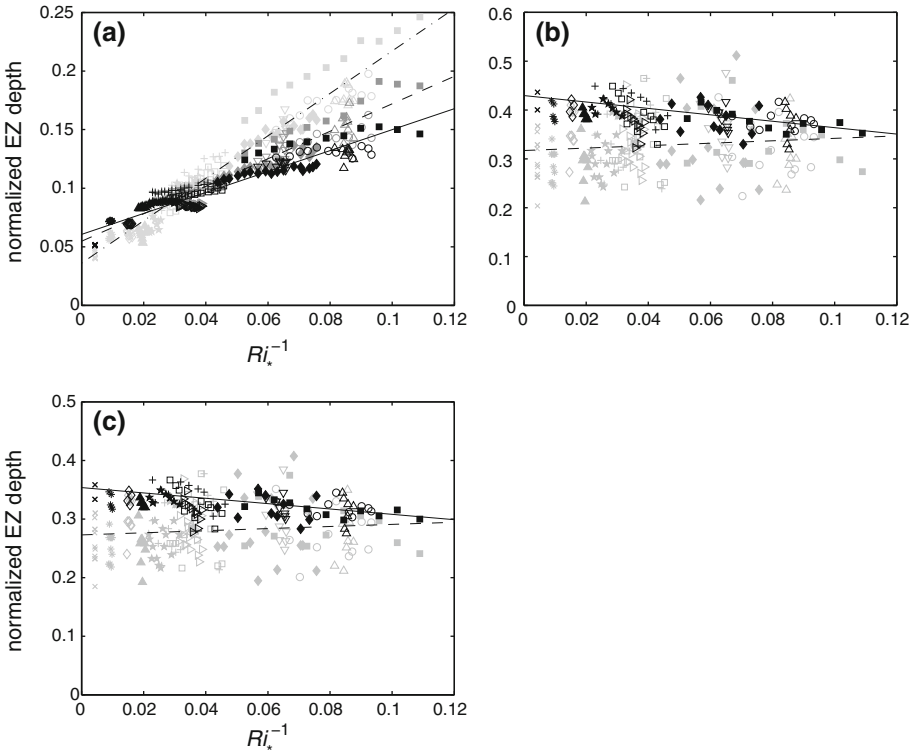

Fig. 5 Normalized entrainment-zone depths plotted against inverse Richardson number: **a** 5–95% limits of the PDF of ABL tops determined from Q profiles scaled by the h_{Qall} (*pale grey*, and *dot-dashed line*), $\langle (h_2 - h_1)/h_1 \rangle$ (*dark grey*, and *dashed line*) and $\langle h_2 - h_1 \rangle / \langle h_1 \rangle$ (*black*, *solid line*); **b** region of negative buoyancy flux scaled by mean level of first zero crossing of the buoyancy flux from instantaneous 3D field (*grey*, *dashed line*) and time-averaged profiles (*black*, *solid line*); **c** as (**b**) but scaled by level of minimum buoyancy flux

Table 5 Coefficients for lines of best fit in Fig. 5

Figure panel/line/dataset	Gradient	Intercept
(a, Pale grey, dash-dot line) 5–95% of PDF/h_{Qall}	1.81±0.06	0.036±0.003
(a, Dark grey, dash line) $\langle (h_2 - h_1)/h_1 \rangle$	1.17±0.05	0.054±0.002
(a, Black, solid line) $\langle (h_2 - h_1) \rangle / \langle h_1 \rangle$	0.89±0.05	0.061±0.002
(b, Black, solid line)	−0.45±0.19	0.41 ± 0.01
(b, Grey, dash line)	0.25±0.34	0.31 ± 0.02
(c, Black, solid line)	−0.31±0.13	0.34 ± 0.01
(c, Grey, dash line)	0.18±0.25	0.27 ± 0.01

extent of the entrainment zone. We now examine the relationship between the mean scalar profile and the entrainment zone more rigorously. Figure 6 shows the value of the gradient in the mean profile at the upper and lower limits of the entrainment zone—as defined by the 5–95% limits of the probability distribution of local ABL top values—as a fraction of the

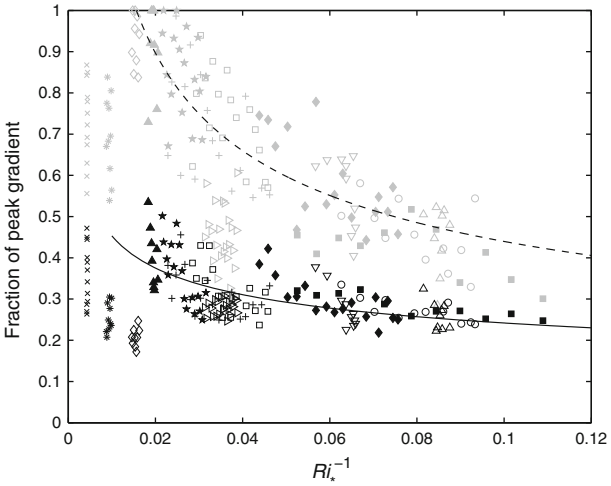

Fig. 6 The vertical gradient of mean scalar profiles as a fraction of the peak gradient at the level of the upper (*grey*) and lower (*black*) limits of the entrainment zone defined by the 5 and 95% limits of the PDF of local ABL tops. Power law *curves* of the form $y = ax^b$ are fit to the upper and lower limits: $a = 0.16 \pm 0.03$, $b = -0.44 \pm 0.05$ (*upper limit*, *dashed line*, excluding runs L, O, Q); $a = 0.13 \pm 0.03$, $b = -0.27 \pm 0.06$ (*lower limit*, *solid line*, excluding runs D, O, Q)

peak gradient, in turn defined by the peak gradient in local tracer profiles. It is clear that the limiting fractional gradients are functions of the inverse Richardson number, and that the upper limit of the EZ shows the greatest variation, decreasing from approximately 2.5 to 1.5 times that at the lower limit as Ri_*^{-1} increases. Both show considerable scatter. Several cases show fractional gradients lying well below the majority—these all correspond to simulations at higher vertical grid resolutions (see Sect. 4.4). Although the limiting values of the gradient vary substantially, the corresponding variation in the altitude is much smaller because of the rapid change in gradient around the transition-zone limits. While the precise values depend on the details of each profile and the vertical grid resolution, in a typical case here the full range of the fraction of the peak gradient for either upper or lower limit correspond to just 4 or 5 grid levels at approximately 12-m increments. Nevertheless, the dependence of the gradient representing the entrainment-zone limits on the inverse Richardson number makes it difficult to apply this approach to determining the entrainment-zone limits in a consistent manner.

4.4 Resolution Sensitivity

Here we examine the sensitivity to grid resolution of the various quantities discussed. There are two distinct resolution sensitivities that may affect the results: the fundamental ability of the model to resolve the entrainment process adequately and the effect of the discretization imposed by the vertical grid interval on the diagnosed values of ABL top, transition zone limits, etc. The former would be expected to adversely affect all the results if the resolution was inadequate; the latter might have an impact on only a subset of the diagnosed quantities. In both cases we assess the adequacy of the resolution by comparing the scaling behaviour across all the simulations. The resolution is assumed adequate to represent the basic entrainment process if the scaling behaviour of the entrainment velocity is consistent with that across a wide range of conditions. Figure 7 shows the normalized entrainment velocity (dh_{Q1}/dt) plotted against inverse Richardson number for all the runs used here, along with a number of

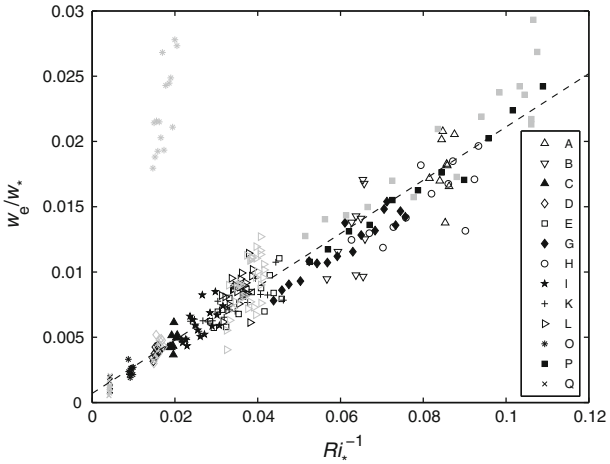

Fig. 7 Normalized entrainment velocity for the simulations used throughout this study (*black symbols*). In *grey* are the results from a number of simulations for identical initial conditions to those with matching *symbols*, but at different resolutions: '×' : J, '∗' : S, '◇' : R, '▷' : N, '■' : F. Full details of each simulation are given in Table 1. The *dashed line* is the fit obtained by Brooks and Fowler (2007)

additional simulations (R, S, N, F, J) which have the same initial conditions as cases D, O, L, P, Q respectively, but at lower resolutions. For cases D, Q, and L the only significant difference resulting from the lower resolution is a greater scatter in the results. For case P, the lower resolution results in both greater scatter and a slightly higher absolute value of the entrainment rate, although the results remain within the range of the dataset as a whole. The low resolution version of case O, (S), however, shows a markedly different behaviour, having a significantly overestimated entrainment rate. Only in this last case, which has a very strong inversion, is the default resolution inadequate to provide a valid estimate of the entrainment rate.

Although the entrainment velocity shows no resolution dependent bias for the cases used throughout this study, there is evidence of an impact on some of the ABL depth and entrainment-zone diagnostics. As noted above for Fig. 6, in several cases the vertical gradient of the area-averaged mean tracer concentration as a fraction of the peak gradient at the entrainment-zone limits are significantly lower than the majority: L, O, and Q for the upper limit and D, O, and Q for the lower limit. These all correspond to high-resolution runs, although not all the high-resolution runs differ from the lower resolution cases. The reason for this difference is twofold: the magnitude of the peak gradient resolved by the model for a given set of conditions is potentially limited by the vertical grid resolution—higher resolution runs are better able to resolve a high vertical gradient; and when identifying a vertical level at which a particular gradient occurs, the available options are again limited by the location of grid levels. Although the difference between the higher and lower resolution runs appears substantial—up to a factor of 2—it represents a difference in altitude of only about 1 vertical grid interval at the lower resolution.

In Fig. 3a–d,f several of the high-resolution runs again show a slight bias relative to the majority of cases, in this case having slightly high values; the discrepancy is 1% or less—less than the vertical grid spacing around the inversion. These small differences are again a result of the limitations on possible values imposed by the discrete grid.

We note that while in the discussion above we have referred to a bias of the results from high-resolution runs with respect to the lower resolution runs; this does not imply any question as to the validity of the results from either set of runs. Rather it emphasizes that, where

features are identified from a discretized vertical profile, the vertical grid intervals impose restrictions on the possible outcomes. Some care should be taken to assess whether such discretization issues might affect calculated quantities or functional relationships, particularly when working with multiple different grids or applying results from one case to another.

In Fig. 4, none of the various estimates of entrainment velocity shows an obvious discrepancy between default and higher resolution runs; however, there is some evidence of discretization. In panels 4c and 4d, and to a lesser extent in 4a and 4b the general trend in normalized entrainment velocity is to increase with inverse Richardson number; within each simulation however the results tend to cluster along lines of slightly decreasing value with Ri_*^{-1} with a trend between clusters of increasing value with Ri_*^{-1}. This behaviour is again interpreted as resulting from the effects of discretization on the possible values of diagnosed quantities. It is notable that this effect is significant only on those diagnostics that use layer-averaged quantities and are thus determined directly on the model grid levels. The results in panels Fig. 4b,f,g use the average of altitudes determined from individual profiles, and do not display the same tendency to cluster results.

5 Conclusions

The approaches applied to identifying boundary-layer top, the entrainment-zone depth, and entrainment velocity from both observations such as lidar backscatter and large-eddy simulations are many and varied. We have examined a range of approaches widely used by previous studies, along with new methods based on recently developed wavelet-based techniques, for large-eddy simulations of the dry convective boundary layer. We have focussed on techniques applicable to lidar backscatter studies, but also included definitions based on the mean buoyancy-flux profile since the region of negative flux is often considered to be a fundamental definition of the entrainment zone. We find that there are some significant differences between the values obtained for all the diagnostic quantities of interest; further that the behaviour of the different definitions with common scaling parameters, such as a convective Richardson number and the convective velocity scale, also differs, sometimes dramatically so. These differences, particularly those of scaling behaviour, make it difficult to directly compare the results of studies utilizing different approaches, and imply that considerable care is required when applying the results of one study to a different dataset. The key conclusions from our study are summarized below:

- Entrainment velocity determination should avoid using ABL depth estimates derived from a single mean profile. The restrictions on possible values imposed by a discrete vertical grid—whether a model grid or lidar range gate—leads to a high degree of scatter and imposes limits on the possible values of calculated entrainment rate that produce bias or may completely mask scaling relationships such as that between w_e/w_* and Ri_*^{-1}. It may also impose resolution dependent biases on calculated diagnostic quantities even where the model resolution is adequate to resolve the entrainment process.
- While there are sound theoretical arguments for using the region of negative buoyancy flux as a diagnostic of the entrainment zone, in practice it differs too much from the measures that can be readily derived from lidar to be useful. It is a much deeper layer than that derived from other approaches, and—being derived from a single domain-averaged profile—suffers from the restrictions imposed by the vertical grid resolution noted above.
- Large-eddy simulation models often provide multiple diagnostic outputs, as in the case of the Met Office LEM used here: time series of domain-averaged quantities, vertical

profiles of quantities averaged both horizontally and over time between outputs, and 3D fields of instantaneous values. There can be significant differences in entrainment properties derived from the time-averaged profiles, and profiles obtained by averaging the instantaneous 3D fields, and in particular very different scaling behaviours. Since single profiles may result in problems resulting from the discrete vertical grid, their use should generally be avoided.

The results of this study complement those of a recent lidar study of entrainment, published while this paper was in revision (Träumner et al. 2011). Using a Doppler lidar they compared ABL depth and entrainment-zone thickness estimates derived from both aerosol backscatter profiles and vertical velocity turbulence statistics, and found significant differences under some conditions. They also assessed the impact of different choices of scaling parameters on various functional relationships such as those between ABL and entrainment-zone length scales and normalized entrainment rate and a modified Richardson number. As here, they found some significant differences in both the degree of correlation and the scaling behaviour.

Acknowledgments AMF was supported by an M.Res. studentship from the UK Natural Environment Research Council at the University of Leeds while undertaking part of this study. Thanks to Wayne Angevine for his thoughtful comments on an early version of the manuscript.

References

Angevine WM (2007) Transitional, entraining, cloudy, and coastal boundary layers. Acta Geophys 56: 2–20. doi:10.2478/s11600-007-0035-1

Angevine WM, White AB, Avery SK (1994) Boundary-layer depth and entrainment zone characterization with a boundary-layer profiler. Boundary-Layer Meteorol 68:375–385

Ayotte KW, Sullivan PP, Andrén A, Doney SC, Holtslag AAM, Large WG, McWilliams JC, Moeng C-H, Otte MJ, Tribbia JJ, Wyngaard JC (1996) An evaluation of neutral and convective planetary boundary layer parameterizations relative to large-eddy simulations. Boundary-Layer Meteorol 79:131–175

Beyrich F (1997) Mixing height estimation from sodar data—a critical discussion. Atmos Environ 31:3941–3953

Beyrich F, Gryning S-E (1998) Estimation of the entrainment zone depth in a shallow convective boundary layer from sodar data. J Appl Meteorol 37:225–268

Boers R, Eloranta EW (1986) Lidar measurements of the atmospheric entrainment zone and the potential temperature junp across the top of the mixed layer. Boundary-Layer Meteorol 34:357–375

Boers R, Eloranta EW, Coulter RL (1984) Lidar observations of mixed layer dynamics: tests of parameterized entrainment models of mixed layer growth rate. J Clim Appl Meteorol 23:247–266

Boers R, Spinhirne JD, Hart WD (1988) Lidar observations of the fine-scale variability of marine stratocumulus clouds. J Appl Meteorol 27:797–810

Brooks IM (2003) Finding boundary layer top: application of a wavelet covariance transform to lidar backscatter profiles. J Atmos Ocean Technol 20:1092–1105

Brooks IM, Fowler AM (2007) A new measure of entrainment zone structure. Geophys Res Lett 34(L16808). doi:10.1029/2007GL030958

Cohn SA, Angevine WM (2000) Boundary-layer height and entrainment zone thickness measured by lidars and wind profiling radars. J Appl Meteorol 39:1233–1247

Coulter RL (1979) A comparison of three methods for measuring mixing-layer height. J Appl Meteorol 18:1495–1499

Davis KJ, Lenschow DH, Oncley SP, Kiemle C, Ehret G, Giez A, Mann J (1997) Role of entrainment in surface–atmosphere interactions over the boreal forest. J Geophys Res 120:29219–29230

Davis KJ, Gamage N, Hagelberg CR, Kiemle C, Lenschow DH, Sullivan PP (2000) An objective method for deriving atmospheric structure from airborne lidar observations. J Atmos Oceanic Technol 17:1455–1468

Deardorff JW, Willis GE, Stockton BH (1980) Laboratory studies of the entrainment zone of a convectively mixed layer. J Fluid Mech 100:41–64

de Haij M, Wauben W, Baltink HK (2007) Continuous mixing layer height determination using the LD-40 ceilometer: a feasibility study. KNMI Report WR 2007-01, 98 pp. http://www.knmi.nl/publications/fulltexts/rp_bsikinsa_knmi_20070117_wr200701.pdf. Accessed 4 Oct 2011

Emeis S, Schäfer K, Münkel C (2008) Surface-based remote sensing of the mixing-layer height—a review. Meteorol Z 17: 621–630. doi:10.1127/0941-2948/2008/0312
Fedorovich E, Conzemius R, Mironov D (2004) Convective entrainment into a shear-free, linearly stratified atmosphere: bulk models reevaluated through large eddy simulations. J Atmos Sci 61:281–295
Ferrare RA, Schols JL, Eloranta EW (1991) Lidar observations of banded convection during BLX83. J Appl Meteorol 30:312–326
Flamant C, Pelon J, Flamant PH, Durand P (1997) Lidar determination of the entrainment zone thickness at the top of the unstable marine atmospheric boundary layer. Boundary-Layer Meteorol 83:247–284
Grabon JS, Davis KJ, Kiemle C, Ehret G (2010) Airborne lidar observations of the transition zone between the convective boundary layer and free atmosphere during the International H^2O Project (IHOP) in 2002. Boundary-Layer Meteorol 134: 61–83. doi:10.1007/s10546-009-9431-1
Hägeli P, Steyn DG, Strawbridge KB (2000) Spatial and temporal variability of mixed-layer depth and entrainment zone thickness. Boundary-Layer Meteorol 97:47–71
Hennemuth B, Lammert A (2006) Determination of the atmospheric boundary layer height from radiosonde and lidar backscatter. Boundary-Layer Meteorol 120: 181–200. doi:10.1007/s10546-005-9035-3
Kiemle C, Ehret G, Davis KJ, (1998) Airborne lidar studies of the entrainment zone. In: AMS, Proceedings 19th international conference on laser radar, Annapolis, Maryland, 6–10 June 1998, pp 395–398
Lammert A, Bösenberg J (2006) Determination of the convective boundary-layer height with laser remote sensing. Boundary-Layer Meteorol 119: 159–170. doi:10.1007/s10546-005-9020-x
Lenschow DH, Krummel PB, Siems ST (1999) Measuring entrainment, divergence, and vorticity on the mesoscale from aircraft. J Atmos Oceanic Technol 16:1384–1400
Lock AP (1998) The parameterization of entrainment in cloudy boundary layers. Q J Roy Meteorol Soc 124:2729–2753
Lock AP, Macvean MK (1999) The generation of turbulence and entrainment by buoyancy reversal. Q J Roy Meteorol Soc 125:1017–1038
Melfi SH, Sphinhirne JD, Chou SH, Palm SP (1985) Lidar observations of the vertically organized convection in the planetary boundary layer over the ocean. J Clim Appl Meteorol 24:806–821
Morille Y, Haeffelin M, Drobinski P, Pelon J (2007) STRAT: an automated algorithm to retrieve the vertical structure of the atmosphere from single channel lidar data. J Atmos Oceanic Technol 24:761–775
Nelson E, Stull RB, Eloranta EW (1989) A prognostic relationship for entrainment zone thickness. J Appl Meteorol 28:885–903
Nicholls S, Turton JD (1986) An observational study of the structure of stratiform cloud sheets: part 2. Entrainment. Q J Roy Meteorol Soc 112:461–480
Piironen AK, Eloranta EW (1995) Convective boundary layer mean depths and cloud geometrical properties obtained from volume imaging lidar data. J Geophys Res 100(D12):25569–25576
Russell LM, Lenschow DH, Laursen KK, Krummel PB, Siems ST, Bandy AR, Thompson DC, Yates TS (1998) Bidirectional mixing in an ACE 1 marine boundary layer overlain by a second turbulent layer. J Geophys Res 103:16411–16432
Sicard M, Perez C, Rocadenbosch F, Baldansano JM, Garcia-Vizcaino D (2006) Mixed-layer depth determination in the Barcelona coastal area from regular lidar measurements: methods, results and limitations. Boundary-Layer Meteorol 119:135–157
Stevens B (2002) Entrainment in stratocumulus topped mixed layers. Q J Roy Meteorol Soc 128:2663–2690
Steyn DG, Baldi M, Hoff RM (1999) The detection of mixed layer depth and entrainment zone thickness from lidar backscatter profiles. J Atmos Oceanic Technol 16:953–959
Sullivan PP, Moeng C-H, Stevens B, Lenschow DH, Mayor SH (1998) Structure of the entrainment zone capping the convective atmospheric boundary layer. J Atmos Sci 55:3042–3064
Träumner K, Kottmeier Ch, Corsmeier U, Wieser A (2011) Convective boundary-layer entrainment: short review and progress using doppler lidar. Boundary-Layer Meteorol. doi:10.1007/s10546-011-9657-6
Tucker SC, Brewer WA, Banta RM, Senft CJ, Sandberg SP, Law DC, Weickmann A, Hardesty RM (2009) Doppler lidar estimation of mixing height using turbulence, shear, and aerosol profiles. J Atmos Oceanic Technol 26:673–688
Wiegner M, Emeis S, Freudenthaler V, Heese B, Junkermann W, Munkel C, Schafer K, Seefeldner M, Vogt S (2006) Mixing layer height over Munich, Germany: variability and comparisons of different methodologies. J Geophys Res 111(D13201). doi:10.1029/2005JD006593
Wilde NP, Stull RB, Eloranta EW (1985) The LCL zone and cumulus onset. J Clim Appl Meteorol 24:640–657
Yi C, Davis KJ, Berger BW, Bakwin PS (2001) Long-term observations of the dynamics of the continental planetary boundary layer. J Atmos Sci 58:1288–1299